Research Square

Preprints are preliminary reports that have not undergone peer review.
They should not be considered conclusive, used to inform clinical practice,
or referenced by the media as validated information.

SAIRA: a Self-consistent Algorithm for spectral Indices measuRements and Analysis

Rogério Riffel

riffel@ufrgs.br

Universidade Federal do Rio Grande do Sul

João P. V. Benedetti

Instituto de Astrofísica de Canarias

Research Article

Keywords: Methods: data analysis, Techniques: spectroscopic, Stellar populations, Galaxies: stellar content, Line: profiles

Posted Date: November 17th, 2026

DOI: https://doi.org/10.21203/rs.3.rs-11367330/v1

License: This work is licensed under a Creative Commons Attribution 4.0 International License.
Read Full License

Additional Declarations: No competing interests reported.

SAIRA: a Self-consistent Algorithm for spectral Indices measuRements and Analysis

Rogério Riffel[1*] and João P. V. Benedetti[2,3]

[1*]Departamento de Astronomia, Instituto de Física, Universidade Federal do Rio Grande do Sul, CP 15051, Porto Alegre, 91501-970, RS, Brazil.
[2]Instituto de Astrofísica de Canarias, Av. Via Lactea s/n, La Laguna, E-38205, Tenerife, Spain.
[3]Departamento de Astrofísica, Universidad de La Laguna, La Laguna, E-38200, Tenerife, Spain.

*Corresponding author(s). E-mail(s): riffel@ufrgs.br;
Contributing authors: joao.pedro.benedetti@iac.es;

Abstract

We present SAIRA (Self-consistent Algorithm for spectral Indices measuRements and Analysis), a PYTHON-based package for measuring equivalent widths, magnitude-defined spectral indices, and spectral breaks with fully self-consistent preprocessing of observational and model spectra. Data are treated to reduce comparison systematics from redshift, wavelength sampling, instrumental line-spread broadening, and stellar velocity dispersion, so that they can be compared with model predictions in an easy way. SAIRA shifts spectra to the rest frame and smooths them to a common (optionally wavelength-dependent) resolution via Fourier-domain Gaussian convolution with variable kernel width, propagating uncertainties through the convolution. The pseudo-continuum is defined by arbitrary bandpasses, and index integrals are computed on each spectrum's native (including non-uniform) wavelength grid. Uncertainties are estimated analytically, from the signal-to-noise ratio of the index or by an exact first-order propagation of the uncertainties in the input spectrum, or via Monte Carlo realisations. SAIRA agrees with the PYLICK code to within $\lesssim$ **0.03** Å, with 95 % of the differences below 0.015 Å, i.e. about 1 % of the typical observational uncertainties. It supports applications from single galaxies to large surveys and integrates into stellar-population fitting pipelines via scripting or a GUI. SAIRA is available at https://github.com/rriffel/saira.

Keywords: Methods: data analysis, Techniques: spectroscopic, Stellar populations, Galaxies: stellar content, Line: profiles

1 Introduction

A central objective in contemporary astrophysics is to elucidate how galaxies assembled their stellar mass over cosmic time. Because the stellar constituents of unresolved systems cannot be examined on a star-by-star basis, constraints on their formation and enrichment histories must be inferred from integrated-light measurements, rendering the analysis of galactic stellar populations an intrinsically inverse problem. Establishing a robust mapping between observables and the underlying physical parameters is, however,

non-trivial: distinct processes and properties (e.g. stellar age, overall metallicity, detailed abundance ratios, and the initial mass function) can yield degenerate spectral signatures. This challenge is further exacerbated by the high dimensionality of galaxy spectra, which typically comprise thousands of wavelength elements, thereby complicating parameter inference and model interpretation.

In this context, measuring the equivalent widths (EWs) of absorption features constitutes one of the most straightforward and robust approaches to address both issues, and it has been extensively employed in studies of galaxy evolution to infer the stellar properties of galaxies (e.g. Faber 1973; Bica and Alloin 1986; Burstein et al. 1988; Worthey et al. 1994; Worthey and Ottaviani 1997; Trager et al. 1998; Vazdekis 1999; Trager et al. 2000; Thomas et al. 2003; Maraston 2005; Riffel et al. 2019; Eftekhari et al. 2025, and references therein). A key factor underlying the success of this methodology is its conceptual and operational simplicity. Specifically, by defining the feature relative to two (or more) pseudo-continuum bandpasses and normalising the spectrum accordingly, one obtains a direct estimate of the feature strength, which can be compared with predictions from individual stellar spectra and/or evolutionary population synthesis (EPS) models. Moreover, because each index typically covers only a narrow wavelength interval, one can select features that optimise sensitivity to a targeted parameter (e.g. age, metallicity, initial mass function, or chemical abundances) while reducing degeneracies with other parameters (e.g. Worthey et al. 1994; Thomas et al. 2003; Conroy 2013), thereby strengthening the connection between observables and the underlying physical quantities.

Spectral indices are highly effective diagnostics in studies of stellar populations. To be meaningful, however, their measurements must be accurate and, above all, consistent between models and observations, so that variations in index strength truly trace differences in the underlying stellar populations rather than mismatched observational effects. In particular, the strength of most spectral features depends on the spectral resolution and on the system's stellar velocity dispersion, while redshift and the specific pixel sampling of each spectrograph modify which part of the spectrum is included within each bandpass (e.g. Kuntschner 2000; Vazdekis et al. 2010). Over the years, several tools have been created to measure line-strength indices (e.g. INDEXF and LECTOR; Cardiel et al. 1998; Vazdekis 1999), including the PACCE code (Perl Algorithm to Compute Continuum and Equivalent widths; Riffel and Borges Vale 2011), developed by our group. Even so, bringing data and models onto a common reference frame is often left to the user, who must depend on ad hoc scripts that can introduce inconsistencies.

In light of the considerations outlined above, we developed SAIRA[1], a PYTHON library for the measurement of spectral indices in both stellar population synthesis models and observed galaxy spectra. The package provides a self-consistent, end-to-end framework that enables direct, like-for-like comparisons between observational measurements and theoretical predictions. SAIRA constitutes a comprehensive rewrite and extension of PACCE (Riffel and Borges Vale 2011); in addition to EWs, it supports the computation of magnitude-based indices, composite indices computation, and spectral break strengths, accommodates an arbitrary number of continuum bandpasses, applies redshift corrections, and performs spectral convolution to a common (optionally wavelength-dependent) resolution while propagating the associated uncertainties. Index uncertainties can be estimated either analytically or via Monte Carlo simulations. In SAIRA, these procedures are executed within a single function call and are applied in an identical manner to both observational data and model spectra.

The remainder of this paper is organized as follows. Section 2 explains how the indices are measured. Section 3 outlines the procedures used to place the data and models on a common frame, and Sec. 4 details the error estimates. The code architecture and its interfaces are described in Sec. 5. In Sec. 6 we compare our measurements to those produced by other codes, and we conclude with final remarks in Sec. 7. A usage example is provided in Appendix A.

[1] https://github.com/rriffel/saira

2 Index measurements

2.1 Index definitions

In SAIRA, each index is specified by: (i) a name; (ii) the boundaries of the central (feature) bandpass, $[\lambda_{0,\mathrm{L}}, \lambda_{1,\mathrm{L}}]$, with width $\Delta\lambda_{\mathrm{L}} = \lambda_{1,\mathrm{L}} - \lambda_{0,\mathrm{L}}$; (iii) a set of $N_{\mathrm{c}} \geq 2$ pseudo-continuum bandpasses, $[\lambda_{0,k}, \lambda_{1,k}]$ for $k = 1, \ldots, N_{\mathrm{c}}$; and (iv) a citation to the original definition (optional). These definitions are loaded from a plain-text file containing one index per line with pipe-delimited fields, for instance

```
Mgb | 5160.125-5192.625 |
      5142.625-5161.375,
      5191.375-5206.375 | (Trager+98)
```

The package includes two template files: one gathering the most widely used optical indices (e.g. Worthey et al. 1994; Worthey and Ottaviani 1997; Trager et al. 1998; Balogh et al. 1999; Serven et al. 2005, 2011), and another with the optical/NIR definitions from Riffel et al. (2019). Users may add new definitions or adjust existing ones as needed for the physical quantities they wish to probe. If the two limits of the central bandpass coincide ($\lambda_{0,\mathrm{L}} = \lambda_{1,\mathrm{L}}$), the index is treated as a spectral break (Sec. 2.5).

2.2 Pseudo-continuum

Real spectra are sampled at discrete points (λ_i, F_i), with $i = 1, \ldots, N$, set by the spectrograph or by the wavelength grid of the models. For each continuum bandpass k we select the pixels with $\lambda_{0,k} < \lambda_i < \lambda_{1,k}$ and add the two band edges, whose fluxes are obtained by linear interpolation of the spectrum, $F(\lambda_{0,k})$ and $F(\lambda_{1,k})$. This ensures that the bandpass is integrated exactly between its nominal limits, independently of where the pixels fall. The mean flux in the band and its central wavelength are then

$$C_k = \frac{1}{\Delta\lambda_k} \int_{\lambda_{0,k}}^{\lambda_{1,k}} F(\lambda)\,\mathrm{d}\lambda, \qquad \lambda_k = \frac{\lambda_{0,k} + \lambda_{1,k}}{2}, \tag{1}$$

where $\Delta\lambda_k = \lambda_{1,k} - \lambda_{0,k}$. For the classical two-band definitions, $C_1 \equiv C_{\mathrm{blue}}$ and $C_2 \equiv C_{\mathrm{red}}$. The pseudo-continuum under the feature is represented by a straight line,

$$F_{\mathrm{c}}(\lambda) = a\,\lambda + b, \tag{2}$$

whose coefficients are obtained by a least-squares fit to the N_{c} points (λ_k, C_k):

$$\begin{aligned} a &= \frac{N_{\mathrm{c}} \sum_k \lambda_k C_k - \sum_k \lambda_k \sum_k C_k}{N_{\mathrm{c}} \sum_k \lambda_k^2 - \left(\sum_k \lambda_k\right)^2}, \\ b &= \frac{\sum_k C_k - a \sum_k \lambda_k}{N_{\mathrm{c}}}. \end{aligned} \tag{3}$$

For $N_{\mathrm{c}} = 2$, Eq. 3 reduces to the usual line connecting the blue and red pseudo-continua,

$$F_{\mathrm{c}}(\lambda) = C_{\mathrm{blue}}\,\frac{\lambda_{\mathrm{red}} - \lambda}{\lambda_{\mathrm{red}} - \lambda_{\mathrm{blue}}} + C_{\mathrm{red}}\,\frac{\lambda - \lambda_{\mathrm{blue}}}{\lambda_{\mathrm{red}} - \lambda_{\mathrm{blue}}}, \tag{4}$$

which follows the Lick/IDS definition (Worthey et al. 1994; Trager et al. 1998). Note that the continuum bandpasses are not required to straddle the feature. If they all fall on the same side of the central bandpass (e.g. near the limit of the spectral range, or if one side is affected by emission lines, telluric residuals, or detector artefacts), the pseudo-continuum is estimated by extrapolating Eq. 2 beneath the feature. Allowing the use of more than two bands is especially advantageous in the NIR, where the continuum is often influenced by molecular absorption bands and telluric residuals (e.g. Riffel et al. 2019).

2.3 Equivalent widths

After defining the pseudo-continuum, the EW of the spectral feature is computed as

$$\mathrm{EW} = \int_{\lambda_{0,\mathrm{L}}}^{\lambda_{1,\mathrm{L}}} \left[1 - \frac{F(\lambda)}{F_{\mathrm{c}}(\lambda)}\right] \mathrm{d}\lambda, \tag{5}$$

such that absorption lines yield positive EWs (in Å), whereas emission lines correspond to negative values. Analogously to the treatment adopted for the continuum bands, the set of pixels within the central bandpass is augmented by the continuum-interpolated fluxes at the bandpass boundaries, $\lambda_{0,\mathrm{L}}$ and $\lambda_{1,\mathrm{L}}$. The integrals in Eqs. 1 and 5 are then evaluated using the trapezoidal rule (SCIPY.INTEGRATE.TRAPEZOID; Virtanen et al.

2020):

$$\mathrm{EW} \simeq \sum_{j=1}^{M-1} \frac{(\lambda_{j+1} - \lambda_j)}{2} \left[R_j + R_{j+1}\right], \qquad R_j = 1 - \frac{F_j}{F_\mathrm{c}(\lambda_j)}. \tag{6}$$

where the index j spans the M sampling points within the central bandpass, including both edges. Because Eq. 6 explicitly accounts for the local wavelength spacing, $(\lambda_{j+1} - \lambda_j)$, the implementation naturally accommodates non-uniformly sampled spectra (e.g. logarithmically rebinned data) without requiring resampling, provided the input $(\lambda_i; F_i)$ pairs are supplied. Optionally, negative EW measurements (e.g. arising from noise in intrinsically weak features or from emission-line infilling) may be truncated to zero.

2.4 Magnitude indices

Broad molecular indices (e.g. Mg_1, Mg_2, TiO_1, and TiO_2) are conventionally reported in magnitudes (Worthey et al. 1994). Accordingly, SAIRA converts the EW to a magnitude-based index via

$$\mathrm{I}_\mathrm{mag} = -2.5 \log_{10} \left(1 - \frac{\mathrm{EW}}{\Delta\lambda_\mathrm{L}}\right), \tag{7}$$

with the associated propagated uncertainty given by

$$\sigma_{\mathrm{I}_\mathrm{mag}} = \frac{2.5}{\ln 10} \frac{\sigma_\mathrm{EW}}{\Delta\lambda_\mathrm{L} - \mathrm{EW}}. \tag{8}$$

Equation 7 is exact when the pseudo-continuum flux F_c is adopted for normalisation, because $1 - \mathrm{EW}/\Delta\lambda_\mathrm{L}$ corresponds to the mean value of F/F_c across the central bandpass. The set of indices to be converted is specified by the user.

2.5 Spectral breaks

Spectral breaks, such as the D4000 (Bruzual A. 1983) and its narrow-band version $\mathrm{D_n4000}$ (Balogh et al. 1999), are measured as the ratio between the mean fluxes (Eq. 1) in the red and blue bandpasses,

$$D = \frac{C_\mathrm{red}}{C_\mathrm{blue}}. \tag{9}$$

Since the code does not change the flux units of the input spectra, if one would like to compute breaks originally defined in F_ν (e.g. Bruzual A. 1983; Balogh et al. 1999), then spectra given in F_ν should be provided.

2.6 Composite indices

Combinations of spectral indices may be derived a posteriori from the measured quantities by specifying user-defined algebraic expressions (one per line), which are evaluated directly on the resulting output table. Commonly used examples include the mean iron index and the metallicity-sensitive composite index $[\mathrm{MgFe}]'$ introduced by Thomas et al. (2003):

$$\langle \mathrm{Fe} \rangle = \frac{\mathrm{Fe5270} + \mathrm{Fe5335}}{2}, \tag{10}$$

$$[\mathrm{MgFe}]' = \sqrt{\mathrm{Mgb}\ (0.72\,\mathrm{Fe5270} + 0.28\,\mathrm{Fe5335})}. \tag{11}$$

More recently, analogous composite indices have been defined in the near-infrared; for instance, Gasparri et al. (2024) proposed the metallicity tracer [AlFeCr],

$$[\mathrm{AlFeCr}] = \sqrt{\mathrm{Al} + 0.5\,\mathrm{Al1} + 1.4\,\mathrm{FeCr}}, \tag{12}$$

which combines the Al I absorption features at 1.31 and 1.67 μm with the blended Fe I+Cr I feature at 1.16 μm.

3 Using data and models in a uniform way

With the advent of EPS models with full spectral predictions (e.g. Bruzual and Charlot 2003; Maraston 2005; Vazdekis et al. 2010, 2016; Conroy 2013; Verro et al. 2022; Millán-Irigoyen et al. 2021), it is now possible to measure the indices directly on the model spectra, instead of relying on fitting functions. With SAIRA, one can easily apply the same methodology to both data and models, allowing a direct, on-the-fly comparison. The operations described below can be applied, in this order, before the indices are measured. Both are optional and must be explicitly activated by the user; in particular, redshifts or resolutions listed in the input table are ignored unless the corresponding correction is switched on.

3.1 Redshift

Observed spectra are brought to the rest frame by

$$\lambda_{\rm rest} = \frac{\lambda_{\rm obs}}{1+z}, \tag{13}$$

where z is taken individually for each spectrum from the input table (column `redshift`). When the spectra are not listed in a table but found in a directory through a file pattern, a single value of z, given by the user, is applied to all of them. No flux rescaling is required, since all the quantities in Sec. 2 are flux ratios.

3.2 Bad pixels

Following the approach of PYLICK (Borghi et al. 2022), pixels that must not be used in the measurements are masked and replaced by a linear interpolation of the adjacent good pixels, a and b,

$$\begin{aligned} F_i &= F_a + (F_b - F_a)\, w_i, \\ \sigma_i^2 &= \sigma_a^2 + \left(\sigma_b^2 - \sigma_a^2\right) w_i, \end{aligned} \tag{14}$$

with $w_i = (\lambda_i - \lambda_a)/(\lambda_b - \lambda_a)$, before any other operation is performed on the spectrum. A pixel is masked when it is flagged in an optional fourth column of the input file (non-zero values), when it falls within one of the wavelength intervals defined by the user (in the rest frame, e.g. emission lines or sky residuals, applied to all spectra), or when its flux is not finite or its uncertainty is not finite or not positive. For each index, the bad pixel ratio within its bandpasses,

$$\mathrm{BPR} = \frac{N_{\rm bad}}{N_{\rm tot}}, \tag{15}$$

where $N_{\rm tot}$ and $N_{\rm bad}$ are the total number of pixels and the number of masked pixels within the central and pseudo-continuum bandpasses, is computed, and the index is not measured (i.e. it is returned as NaN) when the BPR exceeds a threshold defined by the user, or when all the pixels of its central bandpass are masked.

3.3 Spectral resolution

The strength of most absorption features decreases as they are broadened by the instrumental resolution and by the line-of-sight velocity dispersion of the stars. Thus, a meaningful comparison requires that data and models are measured at the same effective resolution. The initial and final resolutions can be given as a velocity dispersion σ ($\mathrm{km\,s^{-1}}$), as a full width at half maximum (FWHM, in Å) or as a resolving power $R = \lambda/\Delta\lambda$, in any combination, and each can be a constant or a function of wavelength (e.g. read from a file with the resolution curve of the models or of the spectrograph). Internally, all of them are converted to a wavelength-dependent FWHM in Å:

$$\begin{aligned} \mathrm{FWHM}(\lambda) &= 2\sqrt{2\ln 2}\,\frac{\sigma}{c}\,\lambda \\ \text{or} \qquad \mathrm{FWHM}(\lambda) &= \frac{\lambda}{R}, \end{aligned} \tag{16}$$

where c is the speed of light and $2\sqrt{2\ln 2} \simeq 2.355$. The resolution of the input spectra can also be given individually for each spectrum in the input table, which is particularly useful to bring a sample of galaxies with different velocity dispersions to a common value.

Since convolution can only degrade the resolution, the spectra are convolved with a Gaussian kernel whose dispersion is given by the quadratic difference between the final and initial resolutions,

$$\sigma_{\rm K}(\lambda) = \frac{\sqrt{\mathrm{FWHM}_{\rm fin}^2(\lambda) - \mathrm{FWHM}_{\rm ini}^2(\lambda)}}{2\sqrt{2\ln 2}}, \tag{17}$$

in Å. If $\mathrm{FWHM}_{\rm fin} < \mathrm{FWHM}_{\rm ini}$ at all wavelengths the code stops with an error, since the requested resolution cannot be reached. Where this happens only in part of the spectrum, the argument of the square root is set to zero and a minimum kernel width of 0.01 Å is adopted, so that these regions are left essentially unchanged. The code also verifies that both an initial and a final resolution were provided before any convolution is attempted.

A convolution with a kernel that varies along the spectrum cannot be performed with a single fast Fourier transform (FFT). To overcome this problem, we have implemented the algorithm of Cappellari (2023, their Algorithm 1; the VARSMOOTH function of PPXF). First, the wavelength axis is stretched so that the kernel has a

constant width. Expressing the kernel in pixels,

$$\begin{aligned} s_i &= \frac{\sigma_{\rm K}(\lambda_i)}{\delta\lambda_i}, \\ \delta\lambda_i &= \left.\frac{{\rm d}\lambda}{{\rm d}i}\right|_i, \end{aligned} \tag{18}$$

a new coordinate is built as

$$\begin{aligned} u_i &= \sum_{j\le i} \frac{s_{\rm max}}{s_j}, \\ s_{\rm max} &= \max_i(s_i), \end{aligned} \tag{19}$$

in which each pixel i is stretched by a factor $s_{\rm max}/s_i$ and, therefore, the kernel has the same width, $s_{\rm max}$, everywhere. The spectrum is linearly interpolated onto a uniform grid of $n = \lceil u_N - u_1 \rceil$ points in u, zero-padded to the next power of two, $N_{\rm FFT} = 2^{\lceil \log_2 n \rceil}$, and convolved in Fourier space using the analytic transform of the Gaussian:

$$\begin{aligned} \hat{F}_{\rm conv}(\omega_k) &= \hat{F}(\omega_k)\, \exp\left(-\frac{\omega_k^2 s_{\rm max}^2}{2}\right), \\ \omega_k &= \frac{2\pi k}{N_{\rm FFT}}, \end{aligned} \tag{20}$$

with $k = 0, \ldots, N_{\rm FFT}/2$, where $\hat{F}$ is the real FFT of the stretched spectrum. The use of the analytic Fourier transform avoids the discretisation errors of a sampled kernel, which become important when the kernel is narrow compared to the pixel size (Cappellari 2017). Finally, the convolved spectrum is transformed back and interpolated onto the original wavelength grid λ_i. This allows the model predictions to be obtained for any (wavelength-dependent) resolution, preventing the loss of information associated with the additional broadening that would be required when a single, worst-case resolution is adopted for the whole spectrum.

3.4 Propagation of uncertainties through the convolution

We have also generalised the algorithm above to deal with error spectra. Following Klein (2021), for uncorrelated pixel uncertainties σ_i a convolution $F'_i = \sum_j K_j F_{i-j}$ yields

$$\sigma_i'^2 = \sum_j K_j^2\, \sigma_{i-j}^2, \tag{21}$$

i.e. actually the variance needs to be convolved with the square of the kernel. For a Gaussian kernel of dispersion s, K^2 is also a Gaussian, with dispersion $s/\sqrt{2}$. Therefore, the error spectrum is propagated by applying the procedure of Sec. 3.3 (Eqs. 18–20) to σ_i^2, with $\sigma_{\rm K} \to \sigma_{\rm K}/\sqrt{2}$, and taking the square root of the result. In the current implementation the squared kernel is normalised to unit area, which preserves the per-pixel variance level of the input spectrum. This choice is conservative: it neglects the reduction of the per-pixel noise produced by the smoothing, which is compensated by the pixel-to-pixel covariance that is introduced by the convolution and that is not accounted for in the subsequent error estimates.

Since all the integrals are computed on the native wavelength grid of each spectrum and the band edges are obtained by interpolation (Sec. 2), no resampling of data or models to a common grid is required. This avoids the additional correlated noise and smoothing introduced by rebinning. The convolution (Sec. 3.3) also returns the spectrum on its original grid.

4 Uncertainties in the EW

SAIRA provides three ways of estimating the uncertainties of the indices, all making use of the error spectrum σ_i, when available (third column of the input files).

4.1 Analytic estimate

Following Vollmann and Eversberg (2006), the uncertainty of an EW measured over a bandpass of width $\Delta\lambda_{\rm L}$ is

$$\sigma_{\rm EW} = \sqrt{1 + \frac{\bar{F}_{\rm c}}{\bar{F}}}\, \frac{\Delta\lambda_{\rm L} - {\rm EW}}{S/N}, \tag{22}$$

where $\bar{F}$ and $\bar{F}_{\rm c}$ are the mean fluxes of the spectrum and of the continuum within the central bandpass, and S/N is the signal-to-noise ratio of the mean flux $\bar{F}$ (i.e. not the signal-to-noise ratio per pixel). From Eq. 5, $\bar{F}/\bar{F}_{\rm c} \simeq 1 - {\rm EW}/\Delta\lambda_{\rm L}$, so

that Eq. 22 can be written as a function of the EW, the bandpass width and the S/N only:

$$\sigma_{\rm EW} = \frac{\sqrt{(2\Delta\lambda_{\rm L} - {\rm EW})\,(\Delta\lambda_{\rm L} - {\rm EW})}}{S/N}. \qquad (23)$$

When an error spectrum is available, the S/N is computed from the M points of the central bandpass, assuming uncorrelated pixel uncertainties, as

$$S/N = \frac{\bar{F}}{\sigma_{\bar{F}}} = \frac{\frac{1}{M}\sum_{j=1}^{M} F_j}{\frac{1}{M}\sqrt{\sum_{j=1}^{M}\sigma_j^2}}, \qquad (24)$$

which, for a spectrum with nearly constant signal-to-noise ratio per pixel, $(S/N)_{\rm pix}$, gives $S/N \simeq \sqrt{M}\,(S/N)_{\rm pix}$. In the absence of an associated error spectrum (e.g. when the data-reduction pipeline does not output per-pixel uncertainties), the noise level is estimated from the blue continuum bandpass. Specifically, a linear model is fitted to the pixels within this band, the root-mean-square (RMS) of the fit residuals is adopted as the noise per pixel, and $S/N = \sqrt{M}\,C_{\rm blue}/{\rm RMS}$. Note that this last estimate is only approximate, since the residuals may also include real spectral structure within the band.

For spectral-break measurements, the corresponding uncertainty is derived by propagating the uncertainties on the mean fluxes in the blue and red bandpasses, $\sigma_{\rm blue}$ and $\sigma_{\rm red}$ (computed as $\sigma_{\bar{F}}$ in Eq. 24, or as the RMS of the residuals divided by the square root of the number of pixels in the band when no error spectrum is available), through Eq. 9:

$$\sigma_D = D\sqrt{\left(\frac{\sigma_{\rm blue}}{C_{\rm blue}}\right)^2 + \left(\frac{\sigma_{\rm red}}{C_{\rm red}}\right)^2}, \qquad (25)$$

under the assumption that the two bandpass measurements are statistically uncorrelated. Although this analytic procedure is computationally efficient, it does not incorporate uncertainty associated with the placement of the pseudo-continuum. This is the default method of SAIRA.

4.2 First-order error propagation

As an alternative analytic estimate, SAIRA can propagate, to first order, the uncertainties of the individual pixels through exactly the same operations used to measure the indices (Sec. 2). The interpolated edges of the bandpasses, the mean fluxes of the continuum bands (Eq. 1), the least-squares pseudo-continuum (Eq. 3) and the fluxes within the central bandpass are all linear combinations of the observed fluxes F_i, and can be written as $F_j = \sum_i L_{ji} F_i$ and $F_{{\rm c},j} = \sum_i P_{ji} F_i$, where j runs over the M points of the central bandpass (including its interpolated edges) and i over the pixels of the spectrum. Writing Eq. 6 as ${\rm EW} = \sum_j t_j\,(1 - F_j/F_{{\rm c},j})$, where t_j are the weights of the trapezoidal rule, its derivatives are

$$\frac{\partial {\rm EW}}{\partial F_i} = \sum_{j=1}^{M} t_j \left(\frac{F_j\,P_{ji}}{F_{{\rm c},j}^2} - \frac{L_{ji}}{F_{{\rm c},j}}\right), \qquad (26)$$

and, for uncorrelated pixel uncertainties σ_i,

$$\sigma_{\rm EW}^2 = \sum_i \left(\frac{\partial {\rm EW}}{\partial F_i}\right)^2 \sigma_i^2. \qquad (27)$$

Similarly, writing the mean fluxes of the continuum bands as $C_k = \sum_i U_{ki} F_i$, the uncertainty of a spectral break (Eq. 9) is

$$\sigma_D^2 = \sum_i \left(\frac{U_{{\rm red},i} - D\,U_{{\rm blue},i}}{C_{\rm blue}}\right)^2 \sigma_i^2. \qquad (28)$$

Unlike the expressions based on the signal-to-noise ratio of the feature (e.g. Cardiel et al. 1998; Vollmann and Eversberg 2006, and Sec. 4.1), Eqs. 26–28 account exactly for the noise in the pseudo-continuum bandpasses, for the position of the pseudo-continuum and for the depth of the feature. We verified with simulated spectra and with the Monte Carlo approach described below that they reproduce the scatter of the measurements to within a few per cent, for both weak and strong features (see also Sec. 6). When no error spectrum is available, the noise per pixel is also estimated as the RMS of the residuals of a linear fit to the pixels of the blue continuum bandpass (of each continuum bandpass, for breaks), and propagated in the same way.

4.3 Monte Carlo simulations

Alternatively, the code generates $N_{\rm MC}$ synthetic spectra by perturbing each pixel of the observed spectrum with a Gaussian deviate scaled by its

uncertainty,

$$F_i^{(m)} = F_i + \sigma_i\,\epsilon_i^{(m)}, \qquad \epsilon_i^{(m)} \sim \mathcal{N}(0,1), \quad (29)$$

with $m = 1, \ldots, N_{\rm MC}$. Pixels with $\sigma_i \leq 0$ (e.g. masked or padded regions) are assigned a negligible uncertainty. All indices are re-measured in each realisation, including the pseudo-continuum, and the uncertainty is taken as the standard deviation of the resulting distribution,

$$\sigma_{\rm EW} = \sqrt{\frac{1}{N_{\rm MC}} \sum_{m=1}^{N_{\rm MC}} \left({\rm EW}^{(m)} - \langle {\rm EW} \rangle\right)^2}, \quad (30)$$

while the index value itself is the one measured in the original spectrum. This approach is slower, but it naturally propagates the noise in the continuum bands, and it is also applied to breaks and magnitude indices (see also Cardiel et al. 1998). When the spectra are convolved, the simulations are performed on the convolved spectrum, using the propagated error spectrum (Sec. 3.4).

5 Code work flow

SAIRA is written in PYTHON and is based only on standard scientific libraries, namely NUMPY (Harris et al. 2020), SCIPY (Virtanen et al. 2020), ASTROPY (Astropy Collaboration et al. 2022), PANDAS (McKinney 2010) and MATPLOTLIB (Hunter 2007). The code is organised in three layers:

- The outermost layer (`saira`) is a wrapper of the inner functions. It only needs as input a list of spectra (either a comma- or tab-separated table (e.g. saved using PANDAS) with a `file` column or a directory and a file pattern), the index definitions and the desired output configuration. The input table can carry, for each spectrum, its redshift (`redshift`) and resolution (`sigma`, `FWHM` or `R`). Indeed, the input table can also host any other information relevant to the science case (e.g. ages, metalicities, magnitudes, etc.). `saira` only appends the columns with the measurements, simplifying the posterior data analysis.; in the directory mode, a single redshift is applied to all spectra. This function handles all the steps, from reading the data to writing the measurements, validates the requested corrections, performs the magnitude conversions and composite indices (Secs. 2.4 and 2.6), and returns a PANDAS DataFrame with each index and its uncertainty (columns `name` and `e_name`), which is also saved as a CSV file.
- The intermediate layer (`eqw`) takes a single spectrum (and error spectrum), applies the corrections described in Sec. 3, and measures all the indices on the clean spectrum, including the error estimates of Sec. 4. This function can be used as a stand-alone routine, e.g. within stellar population fitting codes or other computationally intensive applications.
- The innermost layer comprises the functions that cut the spectrum within the relevant bandpasses and compute the pseudo-continuum (`GetConts`, Eq. 1), the EWs (`computeEW`, Eqs. 2–6) and the breaks (`computeBREAK`, Eq. 9), together with the convolution routines (Sec. 3). Diagnostic plots showing the spectrum before and after the convolution, the bandpasses and the adopted pseudo-continuum can be produced for each index, or for all indices in a single multi-panel figure, to assess the reliability of the continuum placement.

Indices that cannot be measured in a particular spectrum are returned as NaN, without interrupting the run, and columns that are empty for all spectra are removed from the output table. The complete flow of the code, from the input files to the output table, is summarised in Fig. 1.

SAIRA includes a PyQt5-based GUI (Fig. 2) that guides users through its steps (e.g. selecting input files; applying redshift and spectral-resolution corrections; setting error-estimation methods; defining bad-pixel masks; choosing options; and configuring diagnostic plots and outputs). Before running, it checks which indices have central bandpasses outside the spectra's wavelength range and lets users exclude them; the same checks are available via stand-alone functions for scripted use. The GUI also provides interactive index selection, an execution log, and JSON-based save/restore of the full configuration. A plotting tool creates index–index diagrams, supports user-defined algebraic combinations of indices with error bars, and overplots results from multiple files (e.g. data and models). Configurations can also be exported as a stand-alone PYTHON script

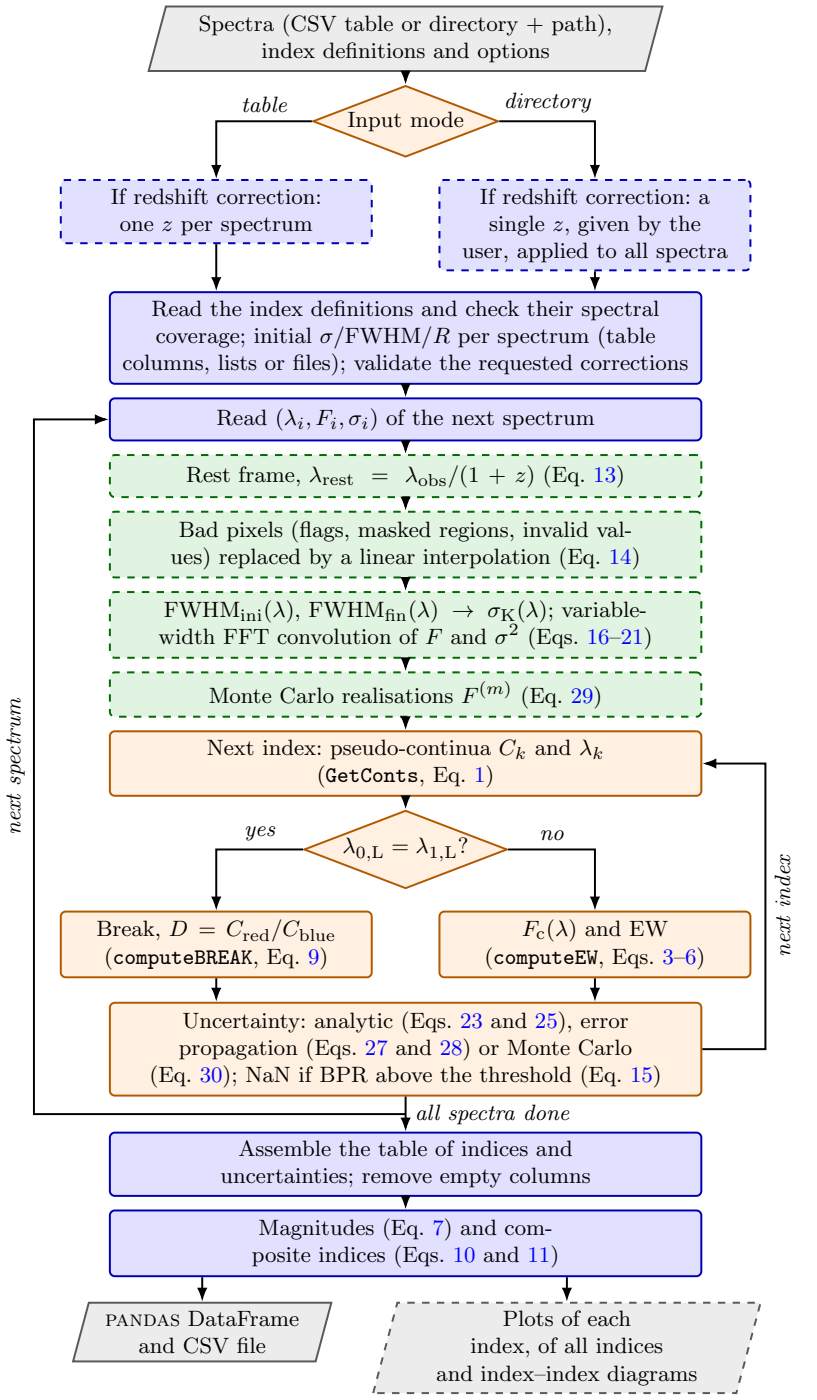


Fig. 1 Flowchart of SAIRA. Blue boxes correspond to the outer layer (the `saira` function), green boxes to the preparation of each spectrum in the intermediate layer (`eqw`), and orange boxes to the inner functions, applied to each index. Dashed boxes are optional steps, performed only when the redshift correction, the resolution change or the Monte Carlo error estimate are requested. Grey boxes show the inputs and outputs. The equations applied in each step are indicated.

that calls `saira` with the same parameters for command-line execution (e.g. on clusters or headless systems); exported and user-written scripts can be re-imported into the GUI. This enables interactive setup with reproducible scripts suitable for automated pipelines without requiring knowledge of the internal codebase.

6 Comparison with other codes

As a first test, we compared the measurements of SAIRA with those of its predecessor, PACCE (Riffel and Borges Vale 2011). We find that both codes produce identical results for all the indices when SAIRA is used without any change of the spectral resolution, an operation that is not available in PACCE. Since PACCE was extensively compared with other methods by Riffel and Borges Vale (2011), the validation presented there also holds for SAIRA.

We also benchmarked SAIRA against the PYTHON package PYLICK[2] (Borghi et al. 2022), adopting the complete set of optical and NIR indices from Riffel et al. (2019) that is provided with SAIRA (Sec. 2.1). For this comparison we employed the 350 E-MILES single stellar population models (Vazdekis et al. 2016) based on Padova isochrones (Girardi et al. 2000), assuming a bimodal IMF with slope 1.30 and solar-scaled abundances, covering ages between 0.063 and 17.8 Gyr and metallicities $-2.32 \leq [\mathrm{M/H}] \leq +0.22$. We measured 45 indices, from Ca4227 to CO2.3b, with both codes on identical spectra and using identical index definitions, at the native model resolution (i.e. with no convolution or redshift correction); all measurements are given in Å. The two youngest, most metal-poor models ([M/H]$= -2.32$, $t = 63$ and 71 Myr) show no flux beyond ∼8950 Å, so we excluded indices whose bandpasses fall on those pixels, resulting in 15 702 measurements. The outcome is presented in Fig. 3. The match is excellent: we find a median offset of $\Delta\mathrm{EW} = \mathrm{EW}_{\mathrm{SAIRA}} - \mathrm{EW}_{\mathrm{PYLICK}} = +0.0000^{+0.0024}_{-0.0026}$ Å (16th–84th percentiles), with a standard deviation of 0.0037 Å; 95 % of the points satisfy $|\Delta\mathrm{EW}| < 0.008$ Å, and the largest discrepancy is 0.027 Å.

In fractional terms, the median $|\Delta\mathrm{EW}|/|\mathrm{EW}|$ equals 0.10 %. For every index, the median differences lie within ±0.01 Å; the largest are for Fe4383 (−0.008 Å), ZrO (+0.007 Å) and Mg_2 (+0.005 Å) (Fig. 3d). The offsets are systematic per index and increase with its EW (Fig. 3b), consistent with the distinct numerical integrations adopted: PYLICK resamples the spectrum to a 0.0625 Å grid and integrates using Simpson's rule, whereas SAIRA applies the trapezoidal rule on the original pixels, interpolating the bandpass limits (Sec. 2.3). Nonetheless, the discrepancies are at least an order of magnitude smaller than the typical observational errors on these indices.

We also tested the two codes on observational data, taking as examples the nine SDSS spectra shipped with SAIRA, for which error spectra, redshifts and velocity dispersions are provided. Each spectrum was shifted to the rest frame using its own redshift while maintaining the native spectral resolution. We then measured the 39 optical EW indices and the $\mathrm{D_n}4000$ break from the second template file distributed with the code (Sec. 2.1), along with their associated uncertainties. The EW comparison is presented in Fig. 4.

As anticipated given the noise level and the SDSS logarithmic wavelength sampling, the scatter is slightly higher than in the model case, yet the agreement remains excellent. The median offset is $\Delta\mathrm{EW} = +0.0014^{+0.0078}_{-0.0049}$ Å, with $\sigma = 0.0068$ Å; 95 % of the measurements satisfy $|\Delta\mathrm{EW}| < 0.015$ Å, and the largest discrepancy is 0.026 Å. The biggest median offsets occur for the broad Mg_2, Mg_1, MgH and aTiO indices (+0.010 to +0.016 Å). Crucially, these differences amount to only ∼1 % of the measurement uncertainties (median $|\Delta\mathrm{EW}|/\sigma_{\mathrm{EW}} = 0.013$). For $\mathrm{D_n}4000$, the median difference is −0.0002, with a maximum value of 0.0003.

Figure 5 compares the different uncertainty estimates. Using as a reference the Monte Carlo uncertainties derived from 500 realisations per spectrum (Sec. 4.3), the analytic prescription of Vollmann and Eversberg (2006) (Sec. 4.1) yields a median ratio of 1.02 and a fairly broad dispersion (16th–84th percentiles: 0.84–1.11). This is expected because it neglects the noise in the pseudo-continuum bandpasses and only approximately captures the feature depth. By contrast, the first-order error-propagation approach (Sec. 4.2) returns a median ratio of 1.00 (0.97–1.03), including for the strongest features. The error estimates from PYLICK, based on Cardiel

[2] https://pylick.readthedocs.io

et al. (1998), are consistently higher by about 15 %: the median ratios of SAIRA to PYLICK uncertainties are 0.88 (0.82–0.93) and 0.87 (0.82–0.94) for the propagated and Monte Carlo uncertainties, respectively, and 0.81 for D_n4000. Lastly, we assessed the handling of bad pixels (Sec. 3.2) by masking, in all SDSS spectra, the rest-frame range 4300–4330 Å and 5 % of randomly chosen pixels with corrupted flux. Using identical masks and BPR thresholds of 1 and 0.3, the two codes reject exactly the same indices, and the EWs of those retained match as closely as in the unmasked case.

7 Final remarks

In this study, we introduce SAIRA, a PYTHON software package developed to measure spectral indices in a self-consistent manner for both observed spectra and stellar population synthesis models. The principal functionalities are summarised below:

- Equivalent widths (EWs), magnitude-based indices, spectral breaks, and composite indices are computed using pseudo-continua defined by an arbitrary number of bandpasses. All integrals are evaluated on the native wavelength grid of each spectrum, thereby naturally accommodating non-uniform spectral sampling.
- Observations and models are placed in a common reference frame via redshift correction and convolution to a shared (potentially wavelength-dependent) spectral resolution. The latter is implemented through a Fourier-domain Gaussian convolution with variable kernel width, and the associated error spectrum is propagated through the convolution step.
- Bad pixels—identified through input flags, located within user-specified wavelength intervals, or exhibiting invalid values—are replaced via linear interpolation. Indices affected by an excessive fraction of bad pixels are excluded from further analysis.
- Uncertainties are quantified using multiple approaches: (i) analytical estimates based on the feature S/N (Vollmann and Eversberg 2006); (ii) first-order propagation of the error spectrum through the same operations used in the index measurements; and (iii) Monte Carlo simulations. The propagated uncertainties are consistent with the Monte Carlo estimates at the level of a few per cent.
- In the absence of resolution matching, indices measured with SAIRA are identical to those obtained with PACCE and agree with measurements from PYLICK to within $\lesssim 0.03$ Å for both stellar population models and observed spectra, corresponding to approximately 1 % of typical observational uncertainties.
- The package can be executed via a single function call, integrated as a collection of standalone functions within external pipelines, or accessed through a graphical user interface.

We anticipate that the public release of this software will facilitate new analyses leveraging spectral indices as observational diagnostics, spanning applications from individual galaxies to large spectroscopic surveys. The code is publicly available on GitHub at https://github.com/rriffel/saira. SAIRA is part of an ongoing effort of the SAFFARY group (Stellar Archaeology, Feeding, Feedback, Abundances, and Resolved spectroscopY in AGN) to provide the community with more intuitive and user-friendly codes for the analysis of astronomical spectra.

Acknowledgements. RR acknowledges support from Conselho Nacional de Desenvolvimento Científico e Tecnológico (CNPq, Proj. CNPq-445231/2024-6,311223/2020-6, 404238/2021-1, and 310413/2025-7), Fundação de amparo à pesquisa do Rio Grande do Sul (FAPERGS, Proj. 19/1750-2 and 24/2551-0001282-6) and Coordenação de Aperfeiçoamento de Pessoal de Nível Superior (CAPES, 88881.109987/2025-01). JPVB acknowledges the support of a fellowship from “la Caixa” Foundation (ID 100010434). The fellowship code is LCF/BQ/DI23/11990084. The Claude artificial intelligence model (Anthropic) was used to assist in the development of the graphical user interface of SAIRA. This work made use of NumPy (Harris et al. 2020), SciPy (Virtanen et al. 2020), Astropy (Astropy Collaboration et al. 2022), pandas (McKinney 2010), Matplotlib (Hunter 2007), PyQt5 and pPXF (Cappellari 2023).

Declarations

- **Funding:** RR acknowledges support from the Brazilian funding agencies CNPq (Proj.

445231/2024-6, 311223/2020-6, 404238/2021-1 and 310413/2025-7), FAPERGS (Proj. 19/1750-2 and 24/2551-0001282-6) and CAPES (88881.109987/2025-01). JPVB acknowledges the support of a fellowship from "la Caixa" Foundation (ID 100010434; fellowship code LCF/BQ/DI23/11990084).

- **Conflict of interest:** The authors declare no conflict of interest.
- **Ethics approval and consent to participate:** Not applicable.
- **Consent for publication:** Not applicable.
- **Data availability:** The SDSS spectra used in this work are publicly available through the SDSS archive, and the E-MILES models through the MILES website. The example spectra and models are also distributed with the code.
- **Materials availability:** Not applicable.
- **Code availability:** SAIRA is publicly available at https://github.com/rriffel/saira under the MIT license.
- **Author contribution:** Both authors contributed to the development of the code, to the analysis and to the writing of the manuscript.

Appendix A Usage example

Here we illustrate how SAIRA can be used to compare observations and models, deriving ages and metallicities from an index–index grid. We use a set of SDSS spectra of red galaxies with known redshifts and velocity dispersions, listed in a CSV table with the columns `file`, `redshift` and `sigma`. The spectra are brought to the rest frame and broadened from their individual velocity dispersions to a common $\sigma = 300\,\mathrm{km\,s^{-1}}$, and the uncertainties are estimated with 100 Monte Carlo realisations:

```
from saira import saira

data = saira(
  filename='sdss_table_example.csv',
  path_to_files='sdss_example/',
  IndexDefs='less_defs.ind',
  do_redshift=True,     # redshift column
  do_resolution=True,   # sigma column
  sigma_fin=300.,
  simulate=100,
  compute_idx='compute.txt',
  output_file='sdss.csv')
```

Exactly the same operations are then applied to the E-MILES single stellar population models (Vazdekis et al. 2016), which are broadened from their nominal resolution (FWHM= 2.51 Å) to the same $\sigma = 300\,\mathrm{km\,s^{-1}}$:

```
models = saira(
  filename='miles_table.dat',
  path_to_files='models/',
  IndexDefs='less_defs.ind',
  do_resolution=True,
  FWHM_ini=2.51,
  sigma_fin=300.,
  compute_idx='compute.txt',
  output_file='models.csv')
```

In both calls, the file `compute.txt` contains the expressions of Eqs. 10 and 11. Since the outputs are PANDAS DataFrames, the model grid can be directly used to interpolate the ages and metallicities of the galaxies in, e.g., the Hβ–[MgFe]$'$ plane. The complete example, as well as notebooks illustrating all the functionalities of the code, are distributed with SAIRA.

References

Astropy Collaboration, Price-Whelan, A.M., Lim, P.L., *et al.*: The astropy project: Sustaining and growing a community-oriented open-source project and the latest major release (v5.0) of the core package. The Astrophysical Journal **935**, 167 (2022) https://doi.org/10.3847/1538-4357/ac7c74

Bica, E., Alloin, D.: A grid of star cluster properties for stellar population synthesis. Astronomy and Astrophysics Supplement Series **66**, 171–179 (1986)

Burstein, D., Bertola, F., Buson, L.M., Faber, S.M., Lauer, T.R.: The far-ultraviolet spectra of early-type galaxies. The Astrophysical Journal **328**, 440 (1988) https://doi.org/10.1086/166304 . Accessed 2024-07-08

Bruzual, G., Charlot, S.: Stellar population synthesis at the resolution of 2003. Monthly Notices of the Royal Astronomical Society

344(4), 1000–1028 (2003) https://doi.org/10.1046/j.1365-8711.2003.06897.x . Accessed 2021-11-16

Borghi, N., Moresco, M., Cimatti, A., Huchet, A., Quai, S., Pozzetti, L.: Toward a better understanding of cosmic chronometers: Stellar population properties of passive galaxies at intermediate redshift. The Astrophysical Journal **927**, 164 (2022) https://doi.org/10.3847/1538-4357/ac3240 arXiv:2106.14894

Balogh, M.L., Morris, S.L., Yee, H.K.C., Carlberg, R.G., Ellingson, E.: Differential galaxy evolution in cluster and field galaxies at z ≈ 0.3. The Astrophysical Journal **527**, 54–79 (1999) https://doi.org/10.1086/308056

Bruzual A., G.: Spectral evolution of galaxies. I. Early-type systems. The Astrophysical Journal **273**, 105–127 (1983) https://doi.org/10.1086/161352

Cappellari, M.: Improving the full spectrum fitting method: accurate convolution with Gauss-Hermite functions. Monthly Notices of the Royal Astronomical Society **466**, 798–811 (2017) https://doi.org/10.1093/mnras/stw3020 . ADS Bibcode: 2017MNRAS.466..798C. Accessed 2022-04-11

Cappellari, M.: Full spectrum fitting with photometry in pPXF: stellar population versus dynamical masses, non-parametric star formation history and metallicity for 3200 LEGA-C galaxies at redshift z ≈ 0.8. Monthly Notices of the Royal Astronomical Society **526**, 3273–3300 (2023) https://doi.org/10.1093/mnras/stad2597

Cardiel, N., Gorgas, J., Cenarro, J., González, J.J.: Reliable random error estimation in the measurement of line-strength indices. Astronomy and Astrophysics Supplement Series **127**(3), 597–605 (1998) https://doi.org/10.1051/aas:1998123 . Accessed 2024-10-02

Conroy, C.: Modeling the Panchromatic Spectral Energy Distributions of Galaxies. Annual Review of Astronomy and Astrophysics **51**(1), 393–455 (2013) https://doi.org/10.1146/annurev-astro-082812-141017 . Accessed 2026-05-13

Eftekhari, E., Vazdekis, A., Riffel, R., Dahmer-Hahn, L.G., Chies-Santos, A.L., Beasley, M.A., Villaume, A., Zanatta, E.: Extragalactic globular cluster near-infrared spectroscopy: II. The stellar population synthesis model zero-point problem extends to the near-infrared. Astronomy and Astrophysics **693**, 238 (2025) https://doi.org/10.1051/0004-6361/202449571 arXiv:2412.13587 [astro-ph.GA]

Faber, S.M.: Variations in Spectral-Energy Distributions and Absorption-Line Strengths among Elliptical Galaxies. The Astrophysical Journal **179**, 731 (1973) https://doi.org/10.1086/151912 . Accessed 2026-04-22

Girardi, L., Bressan, A., Bertelli, G., Chiosi, C.: Evolutionary tracks and isochrones for low- and intermediate-mass stars: From 0.15 to 7 , and from to 0.03. Astronomy and Astrophysics Supplement Series **141**(3), 371–383 (2000) https://doi.org/10.1051/aas:2000126 . Number: 3. Accessed 2021-11-16

Gasparri, D., Morelli, L., Cuomo, V., Ivanov, V.D., Pizzella, A., François, P., Coccato, L., Corsini, E.M., Costantin, L., Dalla Bontà, E., Méndez-Abreu, J., Aguerri, J.A.L.: Near-infrared spectroscopic indices for unresolved stellar populations. III. Composite indices definition as age and metallicity tracers and model comparison. Monthly Notices of the Royal Astronomical Society **530**(1), 560–585 (2024) https://doi.org/10.1093/mnras/stae880

Harris, C.R., Millman, K.J., Walt, S.J., *et al.*: Array programming with NumPy. Nature **585**, 357–362 (2020) https://doi.org/10.1038/s41586-020-2649-2

Hunter, J.D.: Matplotlib: A 2d graphics environment. Computing in Science & Engineering **9**, 90–95 (2007) https://doi.org/10.1109/MCSE.2007.55

Klein, R.: Propagating uncertainties in spectral convolution. Research Notes of the American Astronomical Society **5**, 39 (2021) https://doi.org/10.3847/2515-5172/abe8df

Kuntschner, H.: The stellar populations of early-type galaxies in the Fornax cluster. Monthly

Notices of the Royal Astronomical Society **315**(1), 184–208 (2000) https://doi.org/10.1046/j.1365-8711.2000.03377.x . Accessed 2021-11-17

Maraston, C.: Evolutionary population synthesis: models, analysis of the ingredients and application to high-z galaxies. Monthly Notices of the Royal Astronomical Society **362**(3), 799–825 (2005) https://doi.org/10.1111/j.1365-2966.2005.09270.x . Accessed 2023-02-15

McKinney, W.: Data structures for statistical computing in Python. In: Proceedings of the 9th Python in Science Conference, pp. 56–61 (2010). https://doi.org/10.25080/Majora-92bf1922-00a

Millán-Irigoyen, I., Mollá, M., Cerviño, M., Ascasibar, Y., García-Vargas, M.L., Coelho, P.R.T.: HR-PYPOPSTAR: High-wavelength-resolution stellar populations evolutionary synthesis model. Monthly Notices of the Royal Astronomical Society **506**, 4781–4799 (2021) https://doi.org/10.1093/mnras/stab1969

Riffel, R., Borges Vale, T.: pacce: Perl algorithm to compute continuum and equivalent widths. Astrophysics and Space Science **334**(2), 351–356 (2011) https://doi.org/10.1007/s10509-011-0731-9 . Accessed 2021-11-16

Riffel, R., Rodríguez-Ardila, A., Brotherton, M.S., Peletier, R., Vazdekis, A., Riffel, R.A., Martins, L.P., Bonatto, C., Zanon Dametto, N., Dahmer-Hahn, L.G., Runnoe, J., Pastoriza, M.G., Chies-Santos, A.L., Trevisan, M.: Optical/NIR stellar absorption and emission-line indices from luminous infrared galaxies. Monthly Notices of the Royal Astronomical Society **486**(3), 3228–3247 (2019) https://doi.org/10.1093/mnras/stz1077 . Accessed 2021-11-17

Serven, J., Worthey, G., Briley, M.M.: The Observability of Abundance Ratio Effects in Dynamically Hot Stellar Systems. The Astrophysical Journal **627**(2), 754 (2005) https://doi.org/10.1086/430400 . Accessed 2024-04-19

Serven, J., Worthey, G., Toloba, E., Sánchez-Blázquez, P.: NH AND Mg INDEX TRENDS IN ELLIPTICAL GALAXIES. The Astronomical Journal **141**(6), 184 (2011) https://doi.org/10.1088/0004-6256/141/6/184 . Accessed 2025-12-17

Trager, S.C., Faber, S.M., Worthey, G., González, J.J.: The Stellar Population Histories of Local Early-Type Galaxies. I. Population Parameters. The Astronomical Journal **119**(4), 1645–1676 (2000) https://doi.org/10.1086/301299 . Accessed 2026-04-22

Thomas, D., Maraston, C., Bender, R.: Stellar population models of Lick indices with variable element abundance ratios. Monthly Notices of the Royal Astronomical Society **339**(3), 897–911 (2003) https://doi.org/10.1046/j.1365-8711.2003.06248.x . Accessed 2021-12-03

Trager, S.C., Worthey, G., Faber, S.M., Burstein, D., González, J.J.: Old stellar populations. VI. absorption-line spectra of galaxy nuclei and globular clusters. The Astrophysical Journal Supplement Series **116**, 1–28 (1998) https://doi.org/10.1086/313099

Vazdekis, A.: Evolutionary Stellar Population Synthesis at 2 A Spectral Resolution. The Astrophysical Journal **513**(1), 224–241 (1999) https://doi.org/10.1086/306843 . Accessed 2026-05-13

Vollmann, K., Eversberg, T.: Remarks on statistical errors in equivalent widths. Astronomische Nachrichten **327**, 862–865 (2006) https://doi.org/10.1002/asna.200610645

Virtanen, P., Gommers, R., Oliphant, T.E., *et al.*: SciPy 1.0: fundamental algorithms for scientific computing in Python. Nature Methods **17**, 261–272 (2020) https://doi.org/10.1038/s41592-019-0686-2

Vazdekis, A., Koleva, M., Ricciardelli, E., Röck, B., Falcón-Barroso, J.: UV-extended E-MILES stellar population models: young components in massive early-type galaxies. Monthly Notices of the Royal Astronomical Society **463**(4), 3409–3436 (2016) https://doi.org/10.1093/mnras/stw2231 . Accessed 2021-11-16

Vazdekis, A., Sánchez-Blázquez, P., Falcón-Barroso, J., Cenarro, A.J., Beasley, M.A., Cardiel, N., Gorgas, J., Peletier, R.F.: Evolutionary stellar population synthesis with MILES - I. The base models and a new line index system. Monthly Notices of the Royal Astronomical Society (2010) https://doi.org/10.1111/j.1365-2966.2010.16407.x . Accessed 2023-02-15

Verro, K., Trager, S.C., Peletier, R.F., Lançon, A., Arentsen, A., Chen, Y.-P., Coelho, P.R.T., Dries, M., Falcón-Barroso, J., Gonneau, A., Lyubenova, M., Martins, L., Prugniel, P., Sánchez-Blázquez, P., Vazdekis, A.: Modelling simple stellar populations in the near-ultraviolet to near-Infrared with the X-shooter Spectral Library (XSL). Astronomy and Astrophysics **661**, 50 (2022) https://doi.org/10.1051/0004-6361/202142387

Worthey, G., Faber, S.M., Gonzalez, J.J., Burstein, D.: Old Stellar Populations. V. Absorption Feature Indices for the Complete Lick/IDS Sample of Stars. The Astrophysical Journal Supplement Series **94**, 687 (1994) https://doi.org/10.1086/192087 . ADS Bibcode: 1994ApJS...94..687W. Accessed 2022-04-19

Worthey, G., Ottaviani, D.L.: Hγ and Hδ Absorption Features in Stars and Stellar Populations. The Astrophysical Journal Supplement Series **111**(2), 377 (1997) https://doi.org/10.1086/313021 . Accessed 2022-11-17

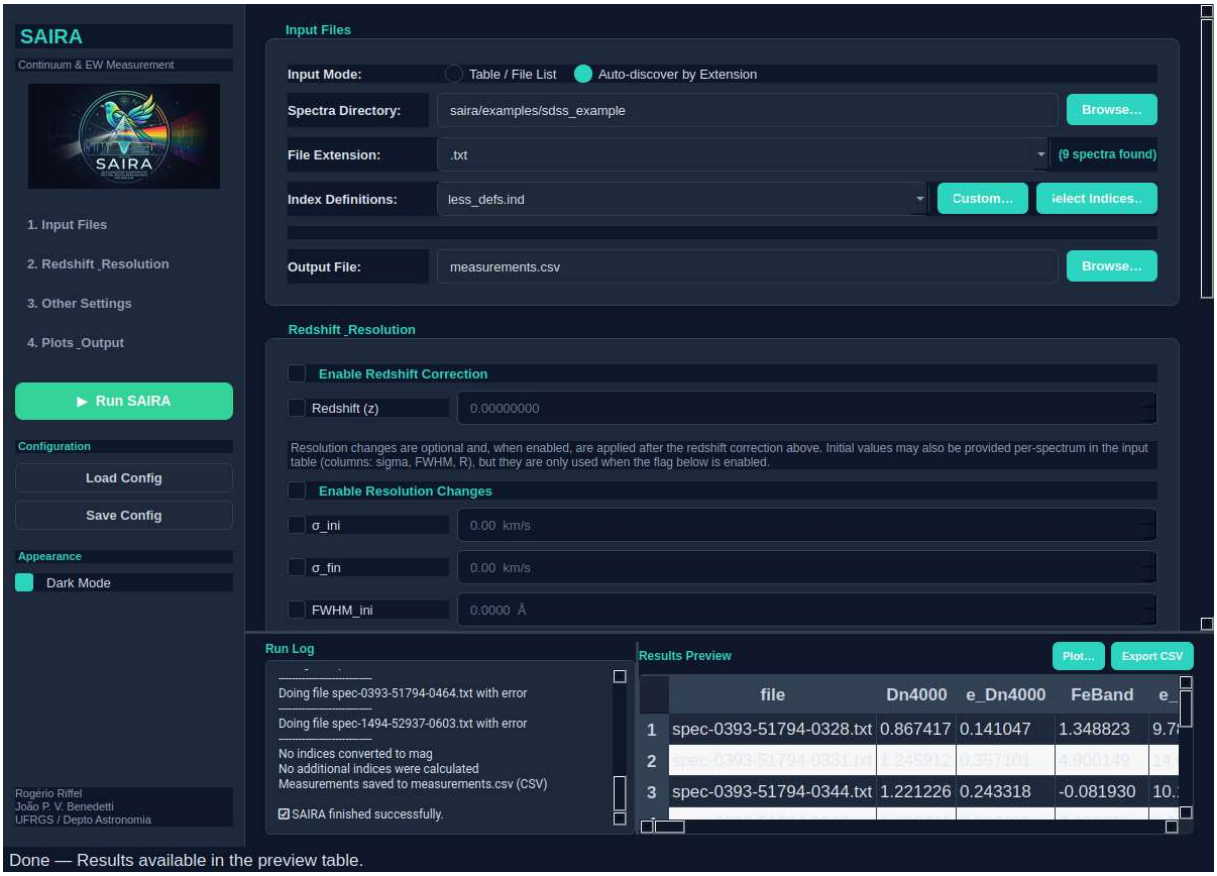


Fig. 2 Main window of the SAIRA graphical user interface. The configuration is organised in four steps: input files (Step 1), redshift and resolution corrections (Step 2), error estimates, magnitude conversion and composite indices (Step 3), and diagnostic plots and output files (Step 4). The run log is shown at the bottom of the window.

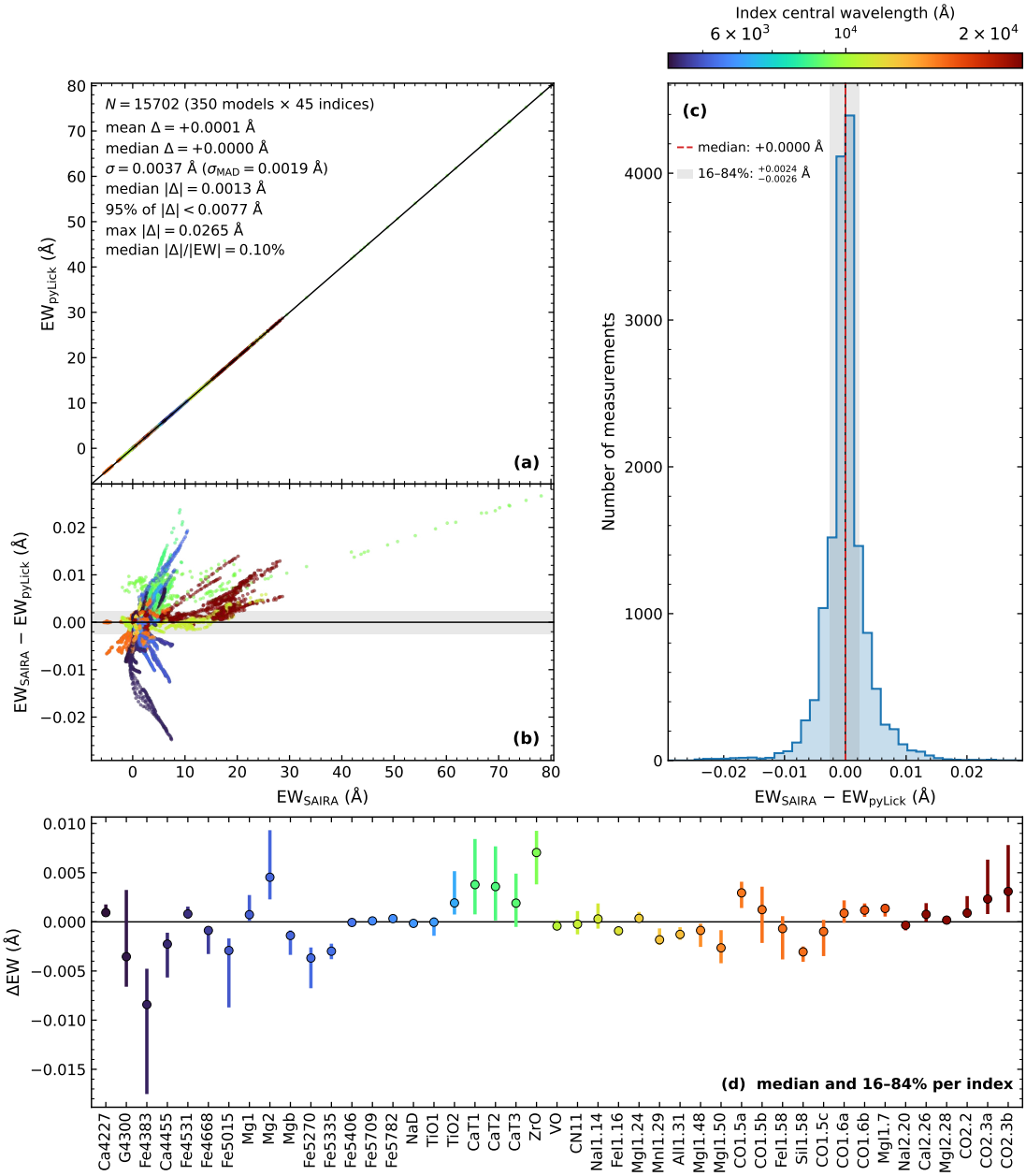


Fig. 3 Comparison of the 45 optical and NIR indices from Riffel et al. (2019) measured using SAIRA and PYLICK across 350 E-MILES single stellar population models at their nominal resolution. Each point corresponds to a measurement and is colour-coded by the index's central wavelength (see colour bar). Panel a: direct one-to-one comparison with the identity line shown in black; summary statistics of the differences appear in the upper left. Panel b: differences versus the EW measured with SAIRA, with the grey shaded region indicating the 16th–84th percentiles. Panel c: histogram of the differences, highlighting the median (red dashed line) and the 16th–84th percentile range (grey band). Panel d: for each index, the median offset (circles) and 16th–84th percentile spread (bars), ordered by wavelength.

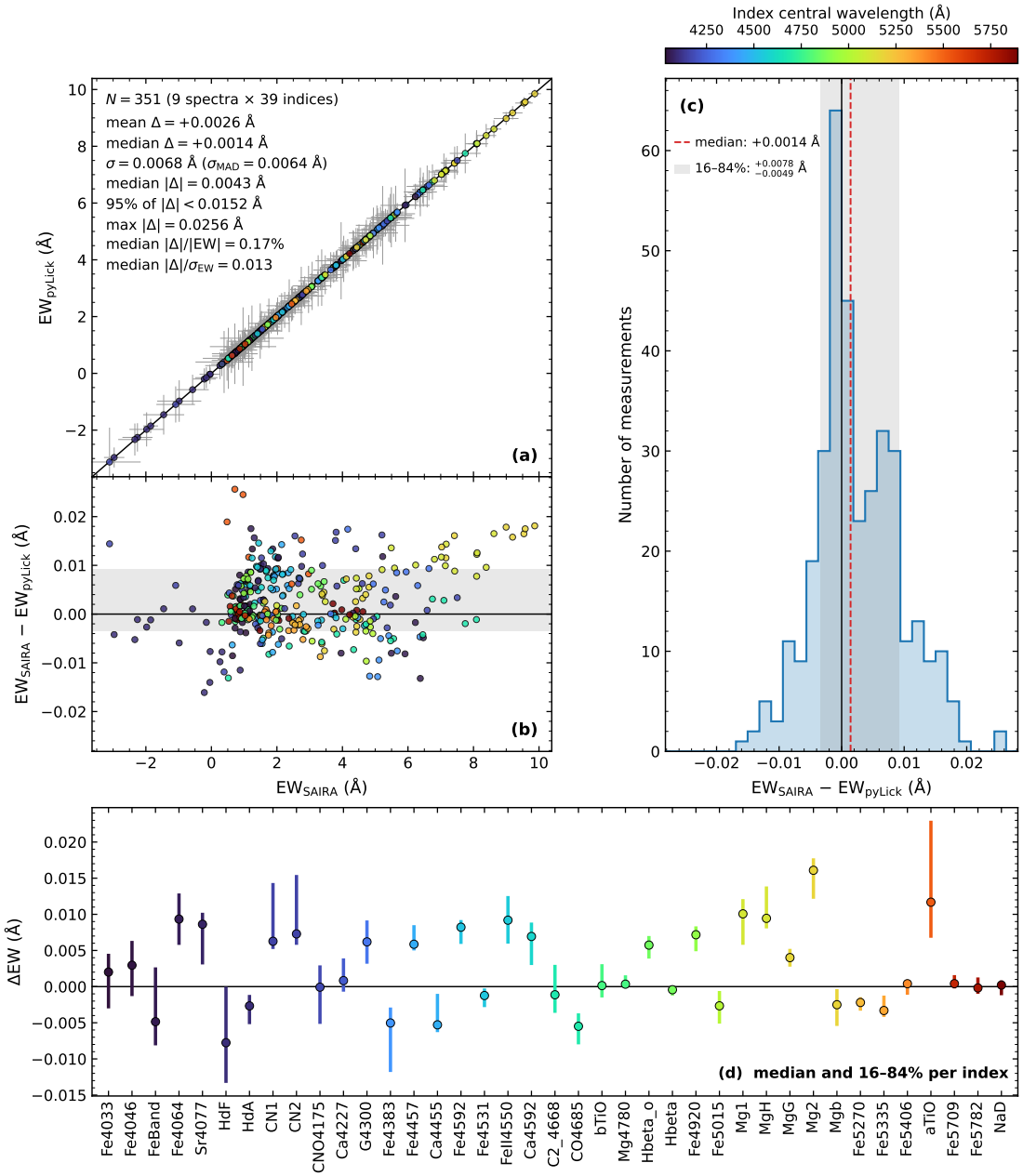


Fig. 4 Same as Fig. 3, but for the 39 optical EW indices measured with SAIRA and with PYLICK in the nine SDSS spectra distributed with SAIRA, in the rest frame and at their original resolution. In panel a, the error bars show the uncertainties of each code, and the statistics include the median ratio between the differences and the SAIRA uncertainties.

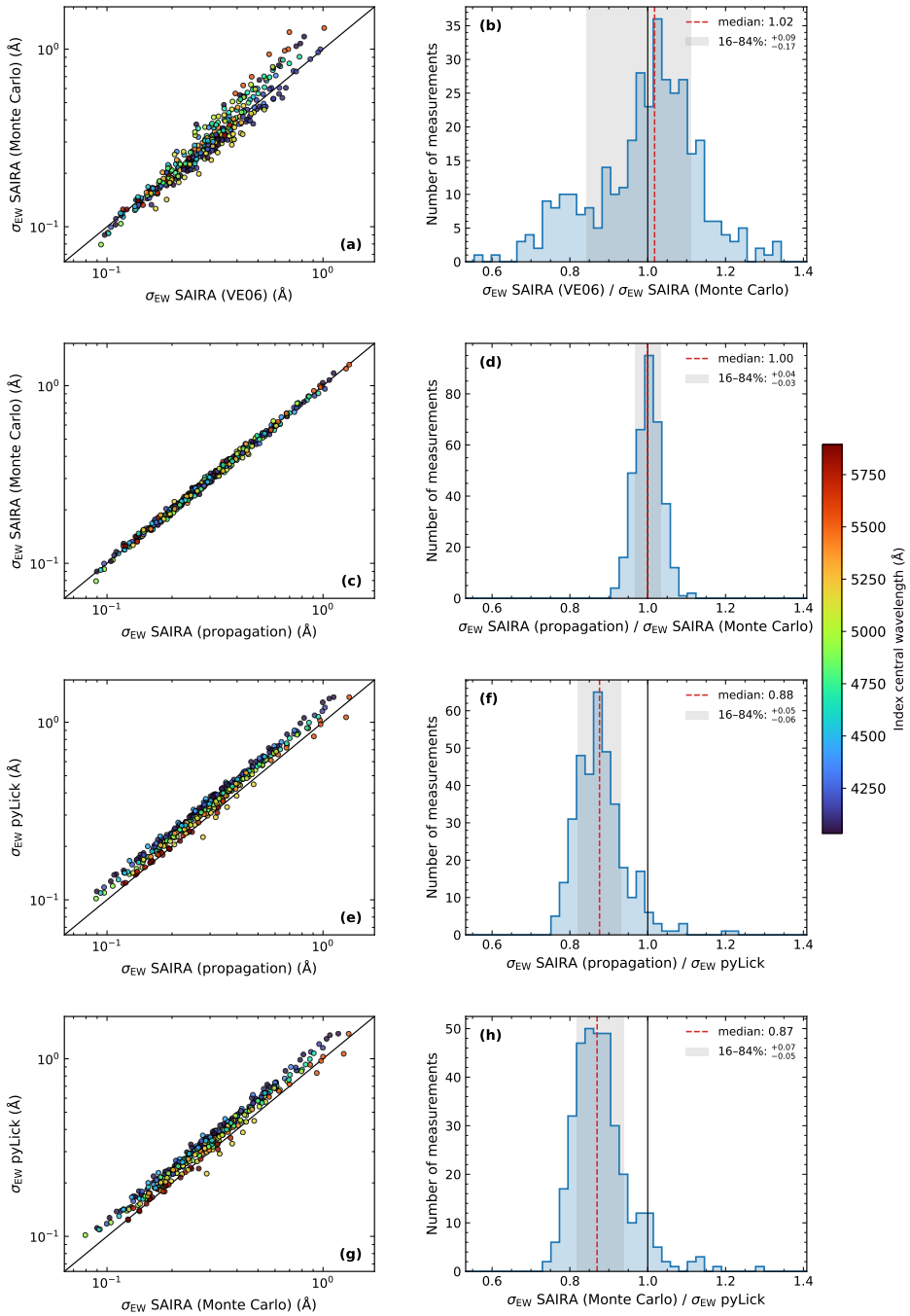


Fig. 5 Comparison between the uncertainties of the EWs shown in Fig. 4. From top to bottom: uncertainties of SAIRA from Vollmann and Eversberg (2006) (Sec. 4.1) and from the first-order error propagation (Sec. 4.2) versus the Monte Carlo uncertainties of SAIRA (500 realisations); and uncertainties of SAIRA from the error propagation and from the Monte Carlo simulations versus those of PYLICK. Left panels show the one-to-one comparison in logarithmic scale, with the identity line in black, and right panels the distribution of the ratios, with the median (red dashed line) and the 16th–84th percentiles (grey band). Points are coloured according to the central wavelength of the index.